THE JOURNAL OF PHYSICAL CHEMISTRY A

Article

Cite This: J. Phys. Chem. A 2019, 123, 7733−7743

pubs.acs.org/JPCA

# The Role of Ozone Vibrational Resonances in the Isotope Exchange Reaction $^{16}O^{16}O + {}^{18}O \rightarrow {}^{18}O^{16}O + {}^{16}O$: The Time-Dependent Picture

Chi Hong Yuen,[†] David Lapierre,[‡] Fabien Gatti,[¶] Viatcheslav Kokoouline,[†] and Vladimir G. Tyuterev*[,‡,§]

[†]Department of Physics, University of Central Florida, Orlando, Florida 32816, United States

[‡]Groupe de Spectrométrie Moléculaire et Atmosphérique, UMR CNRS 7331, UFR Sciences, BP 1039, 51687 Reims Cedex 2, France

[¶]Institut de Sciences Moléculaires d'Orsay, UMR-CNRS 8214, Université Paris-Sud, Université Paris-Saclay, 91405 Orsay, France

[§]QUAMER Laboratory, Tomsk State University, 634000 Tomsk, Russia

Supporting Information

**ABSTRACT:** We consider the time-dependent dynamics of the isotope exchange reaction in collisions between an oxygen molecule and an oxygen atom: $^{16}O^{16}O + {}^{18}O \rightarrow {}^{16}O^{18}O + {}^{16}O$. A theoretical approach using the multiconfiguration time-dependent Hartree method was employed to model the time evolution of the reaction. Two potential surfaces available in the literature were used in the calculations, and the results obtained with the two surfaces are compared with each other as well as with results of a previous theoretical time-independent approach. A good agreement for the reaction probabilities with the previous theoretical results is found. Comparing the results obtained using two potential energy surfaces allows us to understand the role of the reef/shoulder-like feature in the minimum energy path of the reaction in the isotope exchange process. Also, it was found that the distribution of final products of the reaction is highly anisotropic, which agrees with experimental observations and, at the same time, suggests that the family of approximated statistical approaches, assuming a randomized distribution over final exit channels, is not applicable to this case.

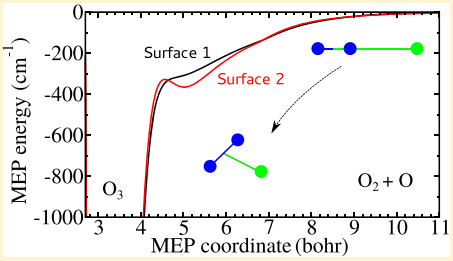


## I. INTRODUCTION

The isotopic exchange reactions that can occur during the collision between an oxygen atom and an oxygen molecule involve, as the intermediate, the metastable ozone $O_3^*$ in excited rovibrational states above the dissociation threshold:

$$O + O_2 \rightarrow O_3^* \rightarrow O_2 + O \quad (1)$$

If a heavy oxygen atom $^{18}O$ hits the symmetric diatomic molecule $^{32}O_2$ composed of two $^{16}O$ atoms, one $^{16}O$ could be kicked out and replaced by isotopic substitution:

$$^{18}O + {}^{16}O^{16}O \rightarrow {}^{50}O_3^* \rightarrow {}^{16}O^{18}O + {}^{16}O \quad (2)$$

However, an adequate modeling of this process represented significant difficulties for theory[1−13] for several decades since the related experimental measurements[14−17] were published.

The probability of this reaction depends on the properties of excited ozone $O_3^*$, which depend on the potential energy surface (PES) supporting the dynamical process.

The ozone PES has been the subject of many ab initio studies over the years (refs 18−27 and references therein) that revealed a complicated electronic structure[20,23,28−30] and rovibrational patterns[31−34] of this seemingly simple triatomic molecule. Extensive spectroscopic works (refs 35−40 and references therein) have been carried out both for remote sensing applications in the atmosphere and for the validation of ab initio predictions in a large spectral range from the fundamental bands up to high overtones and combination rovibrational transitions toward the dissociation threshold.[31,41,42] A description of the ozone formation is among the main incentives for dynamical studies, particularly in the upper atmosphere where the so-called "nascent population"[43] of highly excited vibrational ozone states is not yet well-known. This information is mandatory for a correct interpretation[44,45] of ozone measurements by satellite instruments at conditions of nonlocal thermodynamic equilibrium.

In most studies, it is believed that ozone formation under the stratospheric low-pressure conditions proceeds via a three-body recombination process. According to the Lindemann mechanism, the first step in the recombination, leading to the formation of an excited complex $O + O_2 \rightarrow O_3^*$, which is the same as in eq 1. The second step is a subsequent stabilization by a collision with another partner $O_3^* + M \rightarrow O_3 + M'$, which absorbs an excess of the kinetic energy and makes the metastable complex $O_3^*$ "falling down" into the potential well. Meanwhile, the group of Troe[46,47] has introduced the radical

Received: June 27, 2019
Revised: August 8, 2019
Published: August 13, 2019






DOI: 10.1021/acs.jpca.9b06139
J. Phys. Chem. A 2019, 123, 7733−7743

Table 1. Comparison of Some Key Features of ab Initio PESs of the Ozone Molecule

| | | | | TKTHS[d] | | |
|---|---|---|---|---|---|---|
| | obsd | SSB[a] | AB[c] | NR_PES | R_PES | DLLJG[e] |
| band centers[f] ($cm^{-1}$) | | | | | | |
| $\nu_1$ = (100) | 1103.14 | −1.2[b] | +17.8[b] | 0.0[b] | +1.4[b] | −6.2[b] |
| $\nu_3$ = (001) | 1042.08 | +1.8[b] | +31.7[b] | −0.5[b] | +3.1[b] | +6.7[b] |
| $D_e$[g] (eV) | 1.143[h] | 1.027 | 1.138 | 1.137 | 1.137 | 1.150 |
| calcd − obsd (%) | – | −11.3 | −0.5 | −0.5 | −0.5 | +0.6 |
| $E_{reef}$[i] ($cm^{-1}$) | – | +58 | −102 | – | −320 | – |

[a]PES of Siebert et al.[19,20] [b]Calculated − observed ($cm^{-1}$). [c]PES of Ayouz and Babikov.[25] [d]Two versions of PES of Tyuterev et al.[26] considered in this work. [e]PES of Dawes et al.[27] [f]Fundamental vibrational band. [g]Dissociation asymptotic energy to $O_2(^3\Sigma_g^-)$ + $O(^3P)$. [h]Experimental $D_e$ values obtained from $D_0$ measurement by Ruscic[63] as cited in Holka et al.[22] [i]Reef or barrier on the dissociation MEP with respect to $D_e$.

complex ("chaperon") mechanism,[48] which may also play an important role at higher pressure.

Since the experimental discovery of surprising isotope anomalies in the ozone formation,[49,50] many efforts have been devoted to a theoretical modeling of these processes, but a full understanding of related "strange and unconventional" effects[9,51−55] is still lacking. This involves an unusually high enrichment of heavy isotopomers in the stratosphere and the mass-independent fractionation (MIF) of oxygen isotopes in the ozone formation, which was considered as a milestone in the study of isotope effects.[55] The detailed reviews of the problem can be found in status reports by Schinke et al.,[9] Marcus,[55] and Thiemens.[56] A large symmetry selection in the formation of the ozone molecule required the introduction of ad hoc factors[51,55] to fit observed deviations from a simple statistical behavior. Recent experiments and their modeling[57] have shown that purely statistical theories cannot explain the isotopic effects, which therefore require dynamic state-specific studies. A series of theoretical work performed by the group of Babikov[58−61] explored the role of different types of resonances formed in collisions of O and $O_2$, and showed that the isotope effects could be linked to the formation of Feshbach-type resonances.

The isotopic exchange reaction (1) is in a competition with the ozone formation process and exhibits strong isotopic effects[9,11,12,14−17,62] as well. Because it is only a two-body process, the corresponding dynamics is easier to investigate rigorously. Since both reactions proceed on the same PES, modeling the reaction of eq 2 in the time domain would help in understanding both the dynamics of the isotopic exchange and the ozone recombination, and also would be a step forward in the interpretation of the MIF effects.

In this work, we focus on qualitative state-specific features in wave propagation dynamics in the collisional process (2) related to the formation of the metastable resonances of the excited ozone $O_3^*$. The study aims at better understanding of the impact of the accuracy of the PES in the transition state region, in particular, on the role of a hypothetical "reef" structure on the minimum energy path (MEP) in O + $O_2$ collisions.

## II. POTENTIAL ENERGY SURFACES

Since many previous studies,[8−13,62] it has been recognized that an accurate potential energy surface is a prerequisite for quantum dynamical studies of these processes. A perfect PES must be also applicable for an interpretation of spectroscopic experiments that allow reliable validation of ab initio calculations. It should be able to predict the dissociation threshold and the vibrational bands correctly, and it should have a physically meaningful shape at the transition state (TS) on the way between the molecule and the fragments. Earlier ab initio calculations[18] predicted an activation barrier on the MEP at the TS geometries between $r$ = 3 and $r$ = 5 bohr, where $r$ is the O−O bond distance.

The first accurate global three-dimensional (3D) ab initio PES of the ozone molecule has been constructed by Siebert et al.[19,20] in the group of Schinke, which is usually referred to as the SSB PES.[19] This PES was calculated using the multireference configuration interaction internally contracted (ic-MRCI) method[64] with the Dunning atomic basis set corresponding to the quadruple cardinal number ($l$ = 4) augmented by diffuse functions. The SSB PES predicted quite good low energy frequencies (Table 1), but it has a significant drawback: a strong underestimation of the dissociation energy ($O_2(^3\Sigma_g^-)$ + $O(^3P)$) $D_e$ by about −11%. With respect to the most accurate experimental bond dissociation ($O_3 \rightarrow O_2$ + O) energy $D_0$(obs) = 8485 $cm^{-1}$ calculated by Ruscic et al.[63,65] (as cited in Holka et al.[22]), the $D_0$(SSB) was lower by about 900 $cm^{-1}$. This disagreement was too large for an interpretation of highly sensitive laser absorption experiments[31,37,41] extended up to nearly 93% of $D_0$. With the SSB value for $D_0$, this range would fall in the vibrational continuum of the SSB surface, which is clearly not the case. As in the previous ab initio studies, the SSB PES exhibits a small barrier for the bond O−O length around 4 bohrs of about 50 $cm^{-1}$ above the $D_e$ asymptotic energy.

One-dimensional (1D) and two-dimensional (2D) calculations have shown[7,66] that the barrier would be converted to a "submerged reef" below $D_e$ if larger quintuple ($l$ = 5) or sextuple ($l$ = 6) atomic basis sets were applied. This reef was then followed by a shallow van der Waals (vdW) minimum at larger O−O distances of about 4−5 bohrs. An empirically modified mSSB 3D PES was constructed[21] with the "reef" height $E_{reef}$ = −114 $cm^{-1}$ with respect to the $D_e$ asymptotic energy.

The SSB and mSSB PESs were employed by many groups for the theoretical modeling of the isotope exchange dynamics,[6−9,57,67] using a quantum statistical model, quasi-classical trajectories, and wave propagation method, but it did not produce a satisfactory agreement with observations.[14−17,57]

On the other hand, it was shown that a complete basis set (CBS) limit (either $l$ = 4, $l$ = 5 → ∞,[16,22,25] or $l$ = 5, $l$ = 6 → ∞,[22,26] or $l$ = 3, $l$ = 4 → ∞[23]) was necessary to approach the experimental $D_0$ value.[63,65] At this point, the situation was quite confusing because at the same time the increasing cardinal number of the atomic basis set beyond $l$ = 5 conducted to stretching vibrational $\nu_1$ and $\nu_3$ frequencies, which are significantly larger than the experimental values



DOI: 10.1021/acs.jpca.9b06139
J. Phys. Chem. A 2019, 123, 7733−7743

(Figure 2 in Tyuterev et al.[26]). For example, the Ayouz–Babikov (AB) PES[25] computed with the $l = 4$, $l = 5 \rightarrow \infty$ CBS limit had a correct $D_0$ value exhibiting nearly the same "reef" shape at the TS as the mSSB.[20] However, it overshoots the fundamental $\nu_3$ stretching band center by 31 $cm^{-1}$ with increasing error for the overtone bands, being much less accurate for the spectroscopy than the SSB PES (Table 1).

An important question was whether a reef barrier appeared as an artifact of ab initio approximations presumably caused by an avoided crossing with an excited electronic states.[23] Müller et al. have shown (as cited in ref 26) that the reef would disappear on the 1D MEP if noncontracted MRCI calculations were implemented using the Columbus software.[68] However, a corresponding ansatz was too demanding for a construction of a full 3D PES. Dawes et al.[23] have investigated an impact of the inclusion of several electronic states in the ic-MRCI procedure on the TS range for the ground state. Their first work considered 1D and 2D PES corrections using the $l = 3$, $l = 4 \rightarrow \infty$ CBS extrapolation that changed the shape of the MEP. Dawes et al.[23] have found that due to an optimization of orbitals including several electronic states the reef was transformed to a kind of smooth shoulder. Preliminary estimations using this result together with the approximate quantum statistical model[23] gave possible hints to obtain more consistent temperature dependence of the isotope exchange rates.

Another question concerning the 3D ozone PES was how to combine both a reasonably good $D_e$ and reasonably good vibrations. To this end, two full dimensional ab initio surfaces were constructed by Tyuterev et al.,[26] hereafter referred to as TKTHS PESs. One of the versions has been constructed via hybrid ic-MRCI calculations by sewed results from different atomic basis sets. Within the main $C_{2v}$ well up to the TS, the quintuple atomic basis set (with the cardinal number $l = 5$) was used to ensure reasonably good fundamental vibration frequencies. For the energies above the TS the $l = 5$, $l = 6 \rightarrow \infty$ CBS limit was used to ensure a correct $D_e$ asymptotic energy near the experimental value (Table 1). This first PES was called "R_PES" because it maintained a reef structure, but a much less pronounced one: 3 times lower barrier height $E_{reef} = -320$ $cm^{-1}$ with respect to the $D_e$ than in mSSB[20] or in AB PESs, which had $E_{reef} = -114$ and $-102$ $cm^{-1}$, respectively.

Another TKTHS PES was constructed using a conceptually more consistent ab initio approach. [The FORTRAN subroutine for the TKTHS PES[26] in the symmetry adapted coordinates is available at the S&MPO information system dedicated to ozone spectroscopy via the link http://smpo.univ-reims.fr/files/codes/.] The CBS $l = 5$, $l = 6 \rightarrow \infty$ limit was employed in the entire range of nuclear geometries from the $C_{2v}$ well to the dissociation accounting for 2D "Dawes corrections"[23] on the stretching manifold due to the effect of excited electronic states. The TKTHS ab initio surface constructed in this way was called "NR_PES" (no-reef) because it did not exhibit the reef structure. A comparison of the MEP cuts for these R_PES and NR_PES potentials in the range from the dissociation asymptotic energy to the transition state is shown in Figure 1. The TKTHS[26] NR_PES provides currently the most accurate ab initio predictions for high-resolution spectra assignments: an average error of vibrational bands was about 1 $cm^{-1}$ for various ozone isotopologues[13,31,39−42] measured up to 93% of the dissociation threshold. The validity of the corresponding ab initio ansatz has been recently confirmed by an excellent agreement of predicted band intensities with experiment.[69]

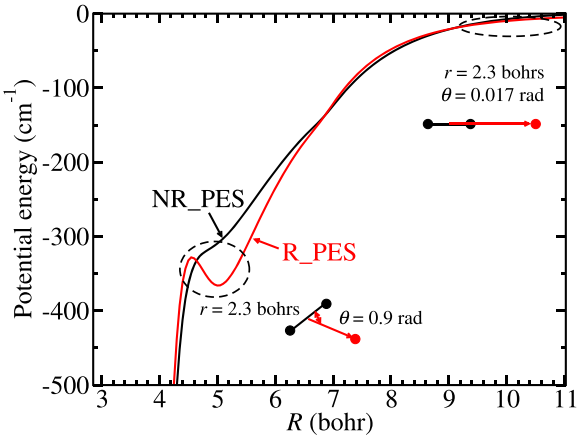


**Figure 1.** Minimum energy pathways of the potential energy surface for R_PES[26] (red lines) and NR_PES[26] (black lines) in Jacobi coordinates.

Later on, Dawes et al.[27] published a full 3D PES (usually referred to as DLLJG PES) using the ansatz of ref 23 and including the long-range interaction part from Lepers et al.[24] and the spin–orbit correction. The DLLJG PES has been employed for the modeling of reaction 2 by Li et al.[10] and by Sun et al.[11] using the time-dependent wave packet method. This permitted for the first time reproduction of a negative temperature dependence of the rate constants, though their predicted absolute values were still underestimated with respect to the observations.[7,14,15,17] These results on the DLLJG PES have been confirmed by Rajagopala Rao et al.[12] using a time-independent approach.

The reader can find a comparison of the MEP cut for various ab initio ozone PESs in Figure 1 of the recent work by Guillon et al.[13] The TKTHS NR_PES[26] was more attractive in the TS range than all other published PESs including that of Dawes et al.[27] Guillon et al.[13] have shown that this NR_PES[26] enabled one to obtain for the first time an excellent quantitative agreement of the theoretical rate coefficient $K_{866}$ with observations.[14−17] Using full quantum mechanical time-independent dynamics calculations, Honvault et al.[62] have published similar work for the theoretical rate coefficient $K_{688}$, but a time-dependent study on this PES, which proved to be accurate both for spectroscopy and for rate constants, has not been yet reported.

## III. WAVE PACKET PROPAGATION USING MULTICONFIGURATION TIME-DEPENDENT HARTREE METHOD

In this work, we show that the time evolution of the wave packet significantly depends even on small topographic features situated relatively deep in the potential well below the dissociation threshold. To this end, we compare time-dependent wave functions obtained using two TKTHS PESs (NR_PES and R_PES described above), which are very similar in the bottom of the $C_{2v}$ well and at the $D_e$ asymptotic energy. A comparison of the high-resolution ozone spectra analyses[31] indicated a clear preference to the NR_PES with respect to the R_PES, but the collisional dynamics on the latter one has not been studied up to now.



DOI: 10.1021/acs.jpca.9b06139
J. Phys. Chem. A 2019, 123, 7733−7743

A previous work of Guillon et al.[13] has shown that the TKTHS NR_PES[26] provides an excellent agreement with the experimental isotope exchange rate (2) using a computationally demanding state-averaging procedure within the time-independent formalism. Here we consider time evolution of the nuclei-exchange process involving a formation of metastable state patterns for the excited ozone $O_3^*$ during the scattering reaction (2) starting from the initial state ($v = 0$, $j = 1$) state of $^{32}O_2$. This brings a supplementary insight in the corresponding state-specific process.

Figure 1 shows the MEP of the NR_PES and the R_PES from Tyuterev et al.[26] along $R$, where $R$ is the distance between the $^{18}O$ atom and the center of mass of the $^{32}O_2$ molecule. The internuclear distance between two $^{16}O$ atoms and the Jacobi angle in the body fixed frame are denoted as $r$ and $\theta$. Along the MEP, $\theta$ takes different values in the circled regions in Figure 1, while $r$ is at the equilibrium distance of the $^{32}O_2$ molecule. One can see that relatively small differences between the values of the NR_PES and R_PES in the reef region are only within 50 $cm^{-1}$. The barrier reef height for the R_PES lies much deeper inside the well ($E_{reef} = -320$ $cm^{-1}$) in comparison with other PESs,[20,21,25] which exhibited either a true barrier or a reef structure and had been used for the dynamics calculations in the previous works.[6−9,57,67] For the mSSB or AB surfaces the reef was only about $-100$ $cm^{-1}$ below $D_e$ (see Table 1). Another important difference is that the R_PES is more attractive on the ozone MEP than the NR_PES just above the TS range (Figure 1), whereas all other published PESs were significantly less attractive than both of them (see Figure 1 of Guillon et al.[13]). Despite the presence of a deeply submerged reef, it is unlikely that the R_PES would support the dynamics in the same way as was reported in earlier works.[6−9,57,67]

To study the time evolution of the wave packet, the multiconfiguration time-dependent Hartree[70−73] (MCTDH) method is used. It is an algorithm to solve the time-dependent Schrödinger equation, which can be considered as a time-dependent version of the multiconfigurational self-consistent field (MCSCF) method applied to the nuclei. Within this method the wave function $\Psi(Q, t)$ of the system is written as a sum of products of *single-particle functions* (SPFs), forming a time-dependent orthonormal basis set. SPFs are low-dimensional functions: When they contain more than one degree of freedom (DOF), the combined coordinates $Q_\kappa \equiv q_{1,\kappa}, ..., q_{d_\kappa,\kappa}$ that comprises $d_\kappa$ physical DOFs are introduced.

The ansatz of the MCTDH wave function reads

$$\begin{aligned}\Psi(Q, t) &= \Psi(q_1, ..., q_f, t)\\ &\equiv \Psi(Q_1, ..., Q_p, t)\\ &= \sum_{j_1}^{n_1} \cdots \sum_{j_p}^{n_p} A_{j_1,...,j_p}(t) \prod_{\kappa=1}^{p} \varphi_{j_\kappa}^{(\kappa)}(Q_\kappa, t)\\ &= \sum_J A_J \Phi_J\end{aligned} \tag{3}$$

where $f$ and $p$ denote the number of degrees of freedom and number of combined modes respectively of the system, $A_J \equiv A_{j_1,...,j_p}$ denotes the MCTDH expansion coefficients, and the configuration or Hartree products $\Phi_J$ are products of SPFs defined in relation 3. The SPFs are finally represented by linear combinations of time independent primitive basis functions as

$$\begin{aligned}\varphi_{j_\kappa}^{(\kappa)}(Q_\kappa, t) &= \varphi_{j_\kappa}^{(\kappa)}(q_{\kappa,1}, ..., q_{\kappa,d_\kappa}, t)\\ &= \sum_{l_1 \cdots l_d} C_{l_1 \cdots l_d}^{(\kappa,j_\kappa)}(t)\, \chi_{l_1}^{(\kappa)}(q_{1,\kappa}) \cdots \chi_{l_d}^{(\kappa)}(q_{d,\kappa})\end{aligned} \tag{4}$$

where the primitive functions $\chi_{l_i}^{(\kappa)}(q_{i,\kappa})$ are usually discrete variable representation (DVR)[74,75] functions with the time-dependent coefficients $C_{l_1 \cdots l_d}^{(\kappa,j_\kappa)}$. The equation of motion for the coefficients and the SPFs are then obtained from the Dirac−Frenkel variational principle. The strength of the method relies on the fact that the number of optimized SPFs used for the propagation is usually much smaller than the number of functions of the primitive basis.

In our particular case, the modes are simply the three nuclear degrees of freedom, $R$, $r$, and $\theta$, and the MCTDH wave function reads

$$\begin{aligned}\Psi(r, R, \theta, t) = \sum_{j_r=1}^{n_r} \sum_{j_R=1}^{n_R} \sum_{j_\theta=1}^{n_\theta} A_{j_r,j_R,j_\theta}(t) \times \varphi_{j_r}(r, t)\\ \times \varphi_{j_R}(R, t) \times \varphi_{j_\theta}(\theta, t)\end{aligned} \tag{5}$$

The number of grid points ($N_r/N_R/N_\theta$) and SPFs ($n_r/n_R/n_\theta$) are given in Table 2: They guarantee a high level of convergence.

**Table 2. Numerical Parameters Used in the MCTDH Calculation**[a]

| | | |
|---|---|---|
| $N_r/N_R/N_\theta$ | 110/210/70 | number of grid points |
| $m_r/m_\theta$ | 29/31 | number of natural potentials |
| $n_r/n_R/n_\theta$ | 17/28/23 | number of single-particle functions |
| $R_{min}/R_{max}$ | 1.0/11.5 | range of $R$ |
| $r_{min}/r_{max}$ | 1.0/6.5 | range of $r$ |
| $(p_0, R_0, w)$ | (−10, 7, 0.2) | momentum, center, and width of $\chi_0$ |
| $\beta_R = \beta_r$ | 3 | order of the CAP |
| $\eta_R/\eta_r$ | $3.25 \times 10^{-4}/1 \times 10^{-4}$ | strength of the CAP |
| $R_c/r_c$ | 7.5/3.5 | starting point of the CAP |
| $L_r = L_R$ | 3 | length of the CAP |
| $T$ | 4000 fs | propagation time |

[a]Parameters are in atomic unit unless specified.

Since the form of the original PES is not adapted to MCTDH, we have utilized the POTFIT[76−78] algorithm to recast the operator in a sum of products of one-dimensional functions. The original multidimensional function is assumed to be given by its values on a multidimensional product grid. POTFIT operates on the grid points only. We thus assume that the values of a potential $V$ are given on a product grid

$$V(\{q\}_{i_1}^{(1)}, ..., \{q\}_{i_p}^{(p)}) = V_{i_1 ... i_p} \tag{6}$$

where $\{q\}_{i_\kappa}^{(\kappa)}$ denotes a grid point of the $\kappa$th coordinate on a grid with $1 \le i_\kappa \le N_\kappa$. Here $N_\kappa$ denotes the number of grid points of the grid for the $\kappa$th coordinate and $p$ is the index for coordinates. Similarly as in MCTDH, the variable $\{q\}$ may be a one-dimensional or multidimensional (i.e., collective) coordinate. Next we define potential density matrices $\varrho^{(\kappa)}$:

$$\varrho_{nm}^{(\kappa)} = \sum_{i_1=1}^{N_1} \cdots \sum_{i_{\kappa-1}=1}^{N_{\kappa-1}} \sum_{i_{\kappa+1}=1}^{N_{\kappa+1}} \cdots \sum_{i_p=1}^{N_p} V_{i_1 ... i_{\kappa-1} n i_{\kappa+1} ... i_p} \times V_{i_1 ... i_{\kappa-1} m i_{\kappa+1} ... i_p} \tag{7}$$



DOI: 10.1021/acs.jpca.9b06139
J. Phys. Chem. A 2019, 123, 7733−7743

and determine their orthonormal eigenvectors, the so-called natural potentials, $\boldsymbol{\nu}_{j_\kappa}^{(\kappa)}$, with components $\nu_{i_\kappa j_\kappa}^{(\kappa)}$ as well as their corresponding eigenvalues $\lambda_{j_\kappa}^{(\kappa)}$ called natural weights. The natural weights are assumed to be in decreasing order, $\lambda_{j_\kappa}^{(\kappa)} \geq \lambda_{j_\kappa+1}^{(\kappa)}$, and we introduce the notation $\nu_{j_\kappa}^{(\kappa)}(\{q\}_{i_\kappa}^{(\kappa)}) := \nu_{i_\kappa j_\kappa}^{(\kappa)}$. We then may now approximate the potential as follows:

$$\begin{aligned} &V(\{q\}_{i_1}^{(1)}, ..., \{q\}_{i_p}^{(p)}) \\ &\approx V^{\mathrm{app}}(\{q\}_{i_1}^{(1)}, ..., \{q\}_{i_p}^{(p)}) \\ &= \sum_{j_1=1}^{m_1} \cdots \sum_{j_p=1}^{m_p} C_{j_1 \cdots j_p} \nu_{i_1 j_1}^{(1)} \cdots \nu_{i_p j_p}^{(p)} \end{aligned} \tag{8}$$

with $m_\kappa \leq N_\kappa$. Here, the expansion coefficients $C_{j_1 \cdots j_p}$ are the overlaps between the potential and the natural potentials

$$C_{j_1 \cdots j_p} = \sum_{i_1=1}^{N_1} \cdots \sum_{i_p=1}^{N_p} V_{i_1 \cdots i_p} \nu_{i_1 j_1}^{(1)} \cdots \nu_{i_p j_p}^{(p)} \tag{9}$$

In order to make the representation as compact as possible, a contraction over the $\nu$th mode is performed. The following functions are defined:

$$D_{j_1 \cdots j_{\nu-1} j_{\nu+1} \cdots j_p}(\{q\}_{i_\nu}^{(\nu)}) = \sum_{j_\nu=1}^{m_\nu} C_{j_1 \cdots j_\nu \cdots j_p} \nu_{i_\nu j_\nu}^{(\nu)} \tag{10}$$

This allows us to rewrite the potential energy surface as

$$\begin{aligned} &V^{\mathrm{app}}(\{q\}_{i_1}^{(1)}, ..., q_{i_p}^{(p)}) \\ &= \sum_{j_1=1}^{m_1} \cdots \sum_{j_{\nu-1}=1}^{m_{\nu-1}} \sum_{j_{\nu+1}=1}^{m_{\nu+1}} \cdots \sum_{j_p=1}^{m_p} \nu_{i_1 j_1}^{(1)} \cdots \nu_{i_{\nu-1} j_{\nu-1}}^{(\nu-1)} \\ &\quad \times D_{j_1 \cdots j_{\nu-1} j_{\nu+1} \cdots j_p}(\{q\}_{i_\nu}^{(\nu)}) \nu_{i_{\nu+1} j_{\nu+1}}^{(\nu+1)} \cdots \nu_{i_p j_p}^{(p)} \end{aligned} \tag{11}$$

and to reduce the number of expansion terms by the factor $m_\nu$. The original potential is exactly reproduced (on the grid points) when $m_\kappa = N_\kappa$. However, a sufficiently accurate approximation of the potential is usually obtained with much smaller values of $m_\kappa$. POTFIT along with MCTDH has already been applied for the calculation of eigenvalues and quantum resonances at a spectroscopic accuracy[79,80] on other systems than $O_3$.

Here, the contracted mode corresponds to the coordinate $R$ and the values of $m_r$ and $m_\theta$ are given in Table 2 resulting in a root-mean-square error on the grid points in the relevant (physical) region of 0.6917 meV.

For total angular momentum $J = 0$, the total Hamiltonian in the body-fixed frame is

$$H = -\frac{1}{2\mu_R}\frac{\partial^2}{\partial R^2} - \frac{1}{2\mu_r}\frac{\partial^2}{\partial r^2} + V(r, R, \theta) \tag{12}$$

$$+ \left(\frac{1}{2\mu_R R^2} + \frac{1}{2\mu_r r^2}\right)\hat{j}^2 \tag{13}$$

where

$$\hat{j}^2 = -\frac{1}{\sin\theta}\frac{\partial}{\partial\theta}\sin\theta\frac{\partial}{\partial\theta} \tag{14}$$

and $\mu_R$ and $\mu_r$ are the reduced mass of the $^{18}O$ atom with respect to the $^{32}O_2$ molecule and the reduced mass of the $^{32}O_2$ molecule, respectively.

In order to compute the flux going into the rearrangement channel and to limit the grid size of the system, two complex absorbing potentials (CAPs) $W_r$ and $W_R$ are introduced into the Hamiltonian,[81−85] such that

$$\tilde{H} = H - i(W_r + W_R) \tag{15}$$

$$W_Q(Q) = \eta_Q h(Q - Q_c)(Q - Q_c)^{\beta_Q} \tag{16}$$

where $Q$ can be $r$ or $R$, $\eta_Q$ is the strength of the CAP, $Q_c$ is the starting point of the CAP, $h(Q - Q_c)$ is the Heaviside step function, and $\beta_Q$ is the order of the CAP.

Together with the Hamiltonian of the system, once the initial wave function is set up, it will be propagated in time and the flux going into the rearrangement channel will be computed.[86] The initial wave function $\Psi_0$ is expressed as the product of a Gaussian wave packet of $^{18}O$ atom $\chi_0(R)$, the vibrational wave function of the $^{32}O_2$ molecule, and the associated Legendre polynomial, which is an eigenfunction of the operator $\hat{j}^2$ with eigenvalue $j_0(j_0 + 1)$. The initial rovibrational state of the dimer is chosen to be $\nu_0 = 0$ and $j_0 = 1$. The initial momentum and width of the Gaussian wave packet are chosen with the initial energy distribution desired, which is given by[87]

$$\Delta(E) = \sqrt{\frac{\mu_R}{2\pi p}} \int_0^\infty \chi_0(R) e^{ipR}\, dR \tag{17}$$

$$p = \sqrt{2\mu_R E} \tag{18}$$

With $\Psi(t) \equiv e^{-i\tilde{H}t}\Psi_0$, the reaction probability is given by

$$P_J(E) = \frac{2}{\pi|\Delta(E)|^2}\,\mathrm{Re}\left(\int_0^\infty g(\tau) e^{iE\tau}\, d\tau\right) \tag{19}$$

$$g(\tau) = \int_0^\infty \langle\Psi(t)|W_r|\Psi(t+\tau)\rangle\, dt \tag{20}$$

The parameters used in our calculation are shown in Table 2. The starting position of the CAP is adjusted such that the tail of the initial wave packet does not overlap with the CAP. The strength of the CAP is selected based on the inspection of the reflected wave packet from the CAP. Propagation time is selected based on the convergence test on the reaction probability at the selected initial wave packet.

## IV. RESULTS AND DISCUSSION

Using eq 20, we compute the probability of reaction 2 with the total angular momentum $J = 0$ using the NR_PES and the R_PES. Figure 2 compares the results obtained using the NR_PES and the R_PES, as well as the results from the time-independent calculation by Guillon et al.[13] The probability obtained with the R_PES has a different fine structure pattern compared to the NR_PES result, mainly due to different positions of resonances present in the collisional spectra for the two surfaces. Also, from the lower panel of Figure 2, one can see that the NR_PES probabilities are, in general, larger than the R_PES result.

The result by Guillon et al. is shifted slightly to adjust the rovibrational energy of the $^{32}O_2$ molecule. We see that from a collision energy larger than 0.034 eV, the result with the NR_PES agrees well with the time-independent calculation. At



DOI: 10.1021/acs.jpca.9b06139
J. Phys. Chem. A 2019, 123, 7733−7743

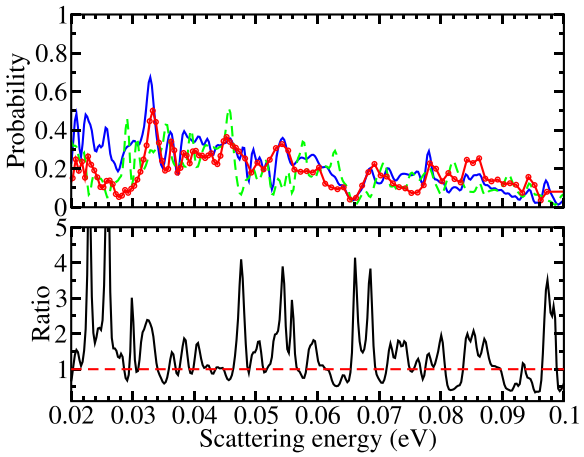


**Figure 2.** (upper panel) Reaction probability for reaction 2 with the total angular momentum $J = 0$, using the NR_PES (blue solid line), R_PES (green dashed line). and results from time-independent calculation from Guillon et al.[13] (red circles). (lower panel) Ratio of the reaction probability computed with the NR_PES to that one obtained with the R_PES.

lower collision energy, positions of resonances in the NR_PES probabilities agree with the time-independent result, but the magnitude is about 50% larger. This is possibly due to the influence of artificial reflections of the low-energy components of the wave packet in the time-dependent calculations. These components are partially reflected from the CAP, which is unable to absorb a wide range of wavenumbers of the outgoing flux. One can overcome this problem by extending the CAP length and the grid, and by lowering the CAP strength. However, this would increase the computational cost significantly. Since we are interested in the dynamics before the fluxes enter the CAP, such improvement is not essential for the present discussion. The agreement between the NR_PES result and the numerically accurate result by Guillon et al. at higher collision energies justifies the validity of the present time-dependent approach at higher energies.

Figure 3 displays the initial probability density of the time-dependent wave function as a function of $(r, R)$ and $(\theta, R)$ respectively. The density function is computed by integrating the wave function $\Psi(r, R, \theta, t)$ over the third coordinate. The PES in the $r-R$ plot has the potential energy path being minimized in $\theta$, while the PES in the $\theta-R$ plot has the potential energy path being minimized in $r$. The contour lines for both PESs begin at $-7161$ cm$^{-1}$ and end at 8903 cm$^{-1}$ with an increment of 2008 cm$^{-1}$. Because the difference between values of the NR_PES and R_PES in the reef region is less than 50 cm$^{-1}$, the contour lines on this scale are indistinguishable among the two PESs. The initial wave packet in the $r-R$ plot is centered at $R = 7$ bohrs with a width 0.5 bohrs while being distributed along $r = 2$ bohrs$-2.5$ bohrs, as the density function is just the product of the vibrational wave function of the $^{32}O_2$ molecule and the Gaussian wave packet $\chi_0(R)$ times a constant. The density function in the $\theta-R$ plot shows similar features along $R$, but delocalized along the range of $\theta$ since the initial rotational quantum number $j_0$ of the $^{32}O_2$ molecule is 1.

Figure 4 shows the time-dependent dynamics of the density function in coordinates $(r, R)$ at $t = 120$, 240, 300, and 440 fs for the NR_PES and R_PES. At $t = 120$ fs, the incoming flux

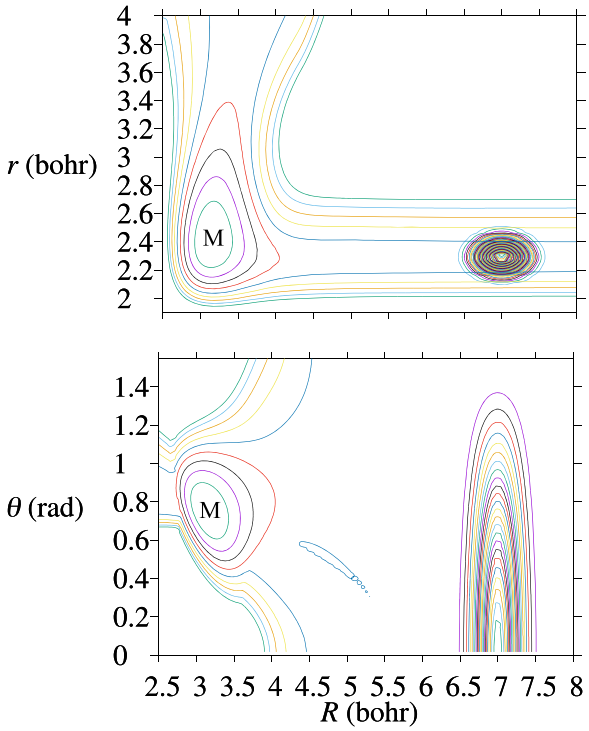


**Figure 3.** Initial density function of the system. The upper panel shows the contour plot on $r$ vs $R$, while the lower panel shows the plot on $\theta$ vs $R$. The location of the $C_{2v}$ minimum of the PES is marked as "M".

arrives at the $C_{2v}$ well without any reflection for both PESs. At $t = 240$ fs, there are more fluxes in the $C_{2v}$ well for the NR_PES than for the R_PES. At $t = 300$ fs, one can see that the incoming fluxes continue to travel to the $C_{2v}$ well for the NR_PES, while significant parts of fluxes are reflected for the R_PES. At $t = 440$ fs, the metastable complex $O_3^*$ in the $C_{2v}$ well begins to decay toward the $^{16}O^{18}O$ molecule. The reflected fluxes in the R_PES are ahead of those in the NR_PES, suggesting that the fluxes with larger kinetic energy are also reflected in the R_PES, but to a lesser extent in the NR_PES.

Figure 5 displays the dynamics of the density function in coordinates $(\theta, R)$ at the same propagation times as in Figure 4. At $t = 120$ fs, the reaction pathway is mainly near $\theta \approx 0.9$ rad, which is consistent with the MEP. An additional feature observed at $t = 240$, 300, and 440 fs is that the reflected flux is localized near $\theta \approx 0$, and moves preferentially along the MEP to exit the interaction region.

Figure 6 shows the expectation value of the coordinate $\langle R \rangle$ for the two surfaces, NR_PES and R_PES, as a function of time. As one can see, the minimum value of $\langle R \rangle \sim 4.5$ bohrs is reached at a time around 150 fs. Before that time the (initially identical) wave packets move along the two surfaces in the same way. During the period of time between 150 and 200 fs the packets are being reflected, such that $\langle R \rangle$ starts to increase, and a time delay between the two wave packets is building up: The wave packet traveling along NR_RES is delayed compared to the R_PES wave packet; i.e., it spends more time in the region of small values of $\langle R \rangle$. The relative time delay is about 20−30 fs, which is about 10% of the total time that the wave packets spend in the region of small $\langle R \rangle$, where reaction 2 of


DOI: 10.1021/acs.jpca.9b06139
J. Phys. Chem. A 2019, 123, 7733−7743

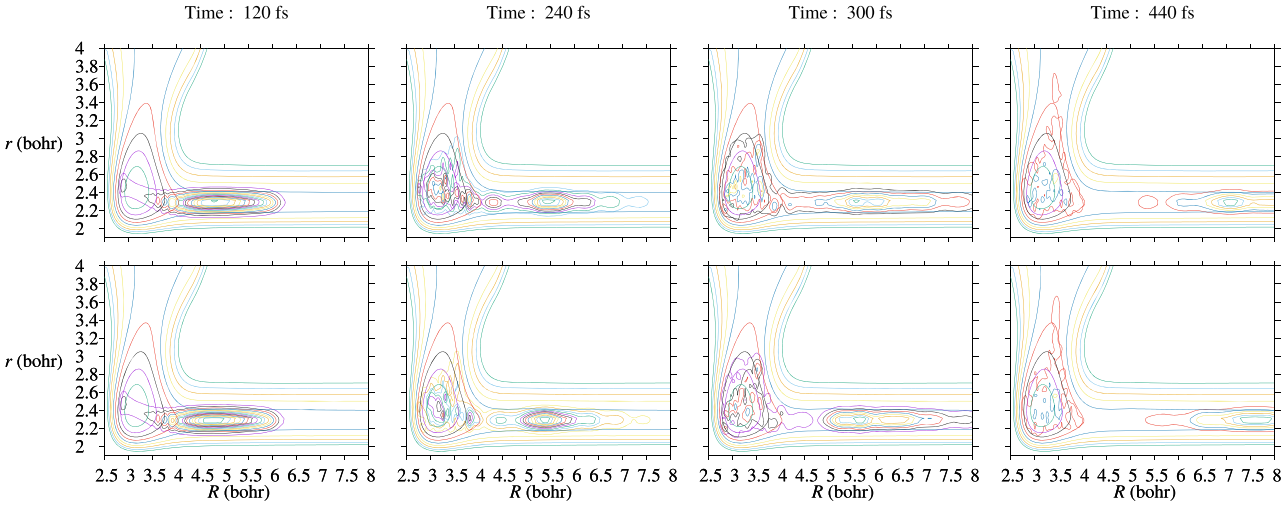


**Figure 4.** Density function of the system in coordinates ($r$, $R$), propagated along the NR_PES (top) and the R_PES (bottom).

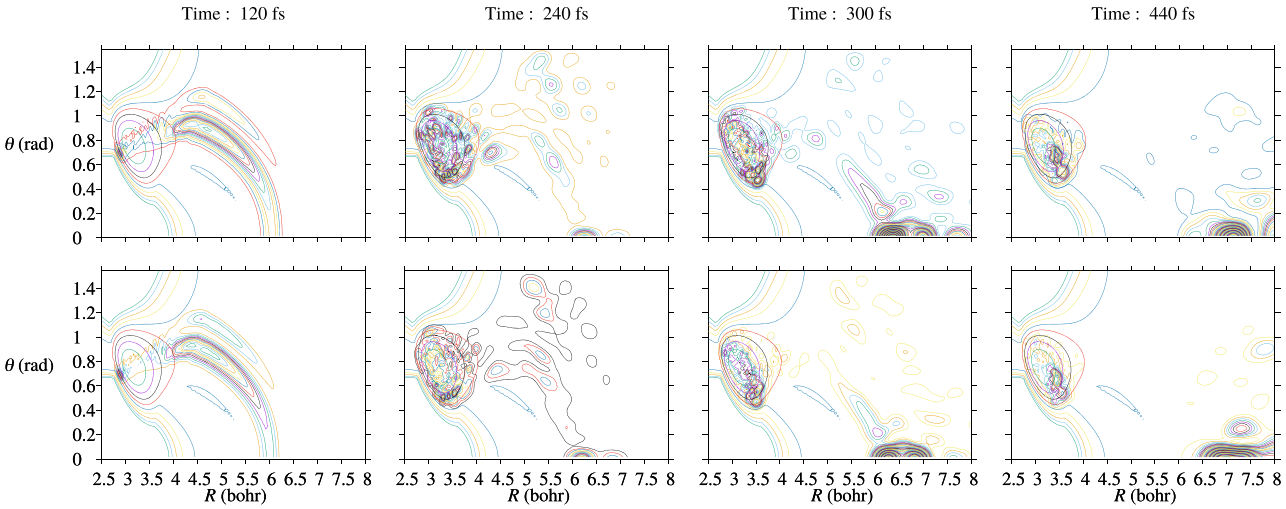


**Figure 5.** Density function of the system in coordinates ($\theta$, $R$), propagated along the NR_PES (top) and the R_PES (bottom).

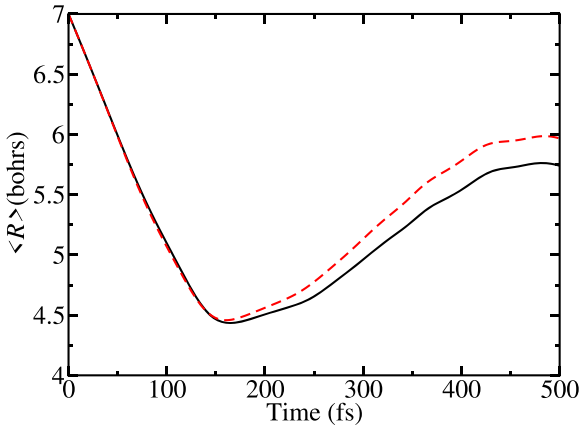


**Figure 6.** Expectation values of the coordinate $R$ for the NR_PES (solid line) and the R_PES (dashed line) versus time.

nuclei exchange takes place. The longer time spent in the interaction region means a larger reaction probability, which is consistent with the results shown in Figure 2.

From the time dynamics of the density functions, one can see that, although the topological difference between the NR_PES and the R_PES is rather subtle, features lying relatively deep in the well could have a significant consequence on the reaction dynamics, thus explaining the result in Figure 2. This gives a hint for understanding why the true or submerged barriers near the $D_e$ asymptote can change the temperature dependence for the thermally averaged rate coefficients.[13] Besides, although there is no barrier along the MEP for the reaction on the two surfaces, reflected fluxes are still observed due to the multidimensional nature of the reaction. Therefore, one can see that an one-dimensional study along the MEP for the reaction does not provide an appropriate picture for the reaction.

Our results also link to the collision time of the reaction, which is essential in some of the statistical approaches for reactive scattering. One[89,90] of such approaches implies that the lifetime of the collision complex is long enough such that the collision complex lives sufficiently long to redistribute the energy of the system randomly between different reaction channels. However, from our results, the time it takes for the system to arrive at the $C_{2v}$ well is about 100 fs, while at about



DOI: 10.1021/acs.jpca.9b06139
J. Phys. Chem. A 2019, 123, 7733−7743

400 fs the complex begins to dissociate. Therefore, the ratio between the average lifetime of the complex to the collision time is ≈ 300/100 = 3, which is not large enough for the assumption of randomized exit channels. For example, the wave packet dynamics shown in Figures 4 and 5 clearly demonstrates that there is a preferential exit channel, along $\theta$ = 0, i.e., along the collinear geometry of $^{34}O_2-^{16}O$, which means that the scattering is very anisotropic and cannot be accounted for by the statistical approaches based on randomized exit channels. An anisotropy in the nuclei-exchange reaction was also observed in the experiment.[8,57,91]

## V. CONCLUSION

In this work, we studied the wave packet dynamics for reaction 2 with $^{32}O_2(v = 0, j = 1)$ and total angular momentum $J = 0$ on the TKTHS PES[26] with and without the reef structure using the MCTDH method. For the NR_PES, a good agreement in the reaction probability at collision energy above 0.034 eV was found between our time-dependent result and the numerically well converged time-independent result obtained by Guillon et al.,[13] who have also used this potential energy surface. But the time-dependent dynamics permits a supplementary insight into the problem.

One of the conclusions of the wave packet propagation concerns the time scale of the process, which in our study is 0.3−0.5 ps for both PESs. This is by an order of magnitude larger than a typical period of O−O bond vibration, confirming the results of the previous works that the exchange reaction (2) is not a direct one-dimensional kick-off process. The resonance scattering states of the intermediate metastable ozone $O_3^*$ corresponding to times 0.24−0.3 ps in Figures 4 and 5 thus play a crucial role for the process. Van Wyngarden et al.[57,67] have observed an anisotropy of angular distribution ("forward bias") of the reaction product in their experiment of crossing O and $O_2$ beams. This feature has also been found in theoretical investigations of the same reaction.[88] According to the interpretation of these experimental and theoretical results, the time scale of the exchange reaction was not sufficient for a full randomization of vibrational energy distribution within the $O_3^*$ complex, which was a necessary condition of a simplified statistical approach.[51,89,90] On the theoretical side, Sun et al.[91] concluded that their state-specific quasi-classical calculations for the trajectories, which have lifetime $t < 2$ ps, would explain this "forward-bias" observation[67] (though they used the symmetry-forbidden $j = 0$ state of $O_2$ for simplicity). Our results provide a quantum mechanical counterpart consistent with these classical trajectory conclusions, as the wave packet reaction time of 0.4 ps in Figure 4 is indeed shorter than the $t < 2$ ps criterion of Sun et al.[91] and could thus contribute to the interpretation of experiments.[57,67]

Our wave packet scattering lifetimes are also consistent with the lifetime distribution of a significant number of vibrational states of metastable ozone $^{48}O_3^*$ (main isotopologue) computed by Lapierre et al.[33] using the NR_PES. However, a full map of the metastable vibrational states of the $^{50}O_3^*$ complex enriched by $^{18}O$ isotope and their lifetimes were not yet calculated.

Another conclusion concerns the impact of the ozone PES shape on the reaction and the scattering resonances of the $O_3^*$ intermediate complex. Both TKTHS PESs[26] are very similar at the bottom of the main $C_{2v}$ well and possess the same dissociation threshold $D_0$. The R_PES has a small submerged barrier much deeper in the well (Table 1) and is more attractive than other PESs possessing the reef structure.[5,21,25,66] The corresponding effect on the dynamics has not been yet used for modeling the exchange reaction (2) in previous studies.

In their quasi-classical study, Janssen et al.[17] have considered the exchange reaction cross section $\sigma$ as a product of two factors, $\sigma = \sigma_{cap}P_{reac}$, where $\sigma_{cap}$ is the capture cross section, i.e., the cross section for trajectories entering the ozone well. Figure 4 shows that, for our quantum wave packet propagation study, $\sigma_{cap}$ is bigger for NR_PES than for R_PES. This is a nontrivial result as the R_PES is more attractive than the NR_PES (Figure 1) at large range distances near the $D_e$ asymptote. A quite small topographic reef feature with the amplitude of about 50 $cm^{-1}$ sitting relatively deep in the well could thus have a significant impact on the reaction probabilities. In general, that the reaction probability is larger for the NR_PES (lower panel of Figure 2) explains the good agreement between experiments and the total reaction rates obtained by Guillon et al.[13] with this PES. At this point we see a correlation between dynamical results and the spectroscopy, as the NR_PES gave clearly more accurate prediction for the observed bands in the energy range approaching the TS.[31]

We found that the topological differences between the NR_PES and the R_PES manifested mainly in the reflection of the wave packet near the reef region. Surprisingly, despite the contrast in the reaction probability between the two PESs, the visible differences in Figures 5 and 6 are subtle as there is only slightly more flux reaching the $C_{2v}$ well for the NR_PES than for the R_PES. Therefore, we concluded that resonance structures and the reaction probability of reaction 2 depend sensitively on the topological structure of the PESs, which is consistent with the conclusion by Guillon et al.[13] Consequently, since the formation of ozone at low pressure proceeds mainly through the Lindemann mechanism, which involves the metastable $O_3^*$, we expect that the three-body recombination rate coefficient at low pressure may also critically depend on the shape of the ozone PES. It is therefore important to use an accurate PES to calculate resonance energies and widths of metastable $O_3^*$ with different isotopic substitutions. To this end, new spectroscopic measurements and assignments of $^{16}O^{16}O^{18}O$ and $^{16}O^{18}O^{16}O$ ozone isotopomers in the energy range near the dissociation threshold would be extremely helpful to validate ab initio PESs.

Ultimately, using reliable calculations of scattering resonance energies and widths of the metastable $^{48}O_3^*$ complex enriched by $^{18}O$ isotope (not yet available on spectroscopically accurate PESs), one should be able to explain the MIF effect,[49,50,62] which is the major challenge for the ozone formation dynamics.[9,46−48,51,54,55] In this context an investigation of long-lived resonances will be important, for example, those linked to the "roaming" nuclear motion[92,93] considered in the classical orbit studies by Mauguière et al.[94]

Although the present results suggest that the assumption about the random distribution over exit channels, used in previous statistical approaches[51,55] applied to $O_3$, is not appropriate for the $^{32}O_2 + {}^{18}O \rightarrow {}^{34}O_2 + {}^{16}O$ reaction, the other types of statistical approaches, taking into account the branching ratios over the final channels, may be appropriate and can simplify significantly the dynamics of $O + O_2$ collisions and the ozone formation in three-body collisions. Theoretical studies, taking advantages of quantum scattering and some reasonable statistical assumptions, describing the ozone



DOI: 10.1021/acs.jpca.9b06139
J. Phys. Chem. A 2019, 123, 7733−7743

dynamics and the dynamics of three-body collisions, such as $O_2 + O + N_2 \rightarrow O_3 + N_2$, are highly desirable.

## ■ ASSOCIATED CONTENT

### Supporting Information

The Supporting Information is available free of charge on the ACS Publications website at DOI: 10.1021/acs.jpca.9b06139.

Movies of the density function of the system in ($r$, $R$) and ($\theta$, $R$), propagated along the NR_PES of the TKTHS PES (ZIP)

## ■ AUTHOR INFORMATION


### Corresponding Author

*E-mail: vladimir.tyuterev@univ-reims.fr.

### ORCID

Chi Hong Yuen: 0000-0002-0544-4976


### Notes

The authors declare no competing financial interest.

## ■ ACKNOWLEDGMENTS

V.K. and V.G.T. acknowledge support from Russian Science Foundation Grant No. 19-12-00171. V.K. and C.H.Y. were partially supported by National Science Foundation Grant No. PHY-1806915.

## ■ REFERENCES


(1) Stace, A. J.; Murrell, J. N. Dynamics of the oxygen exchange reaction. *J. Chem. Soc., Faraday Trans. 2* **1978**, *74*, 2182−2186.

(2) Varandas, A.; Murrell, J. Dynamics of the $^{18}O + {}^{18}O_2$ ($v = 0$) exchange reaction on a new potential energy surface for ground-state ozone. *Chem. Phys. Lett.* **1982**, *88*, 1−6.

(3) Gross, A.; Billing, G. D. Rate constants for ozone formation and for isotopic exchange reactions. *Chem. Phys.* **1993**, *173*, 393−406.

(4) Troe, J. Theory of thermal unimolecular reactions at low pressures. II. Strong collision rate constants. Applications. *J. Chem. Phys.* **1977**, *66*, 4758−4775.

(5) Chajia, M.; Jacon, M. Hemiquantal study of the isotopic exchange reaction $O^{18}(^3P) + O^{16}O^{16}(^3\Sigma_g^-) \rightarrow O^{18}O^{16}(^3\Sigma_g^-) + O^{16}(^3P)$. *J. Chem. Phys.* **1994**, *101*, 271−282.

(6) Yeh, K.-L.; Xie, D.; Zhang, D. H.; Lee, S.-Y.; Schinke, R. Time-dependent wave packet study of the $O + O_2$ ($v = 0$, $j = 0$) exchange reaction. *J. Phys. Chem. A* **2003**, *107*, 7215−7219.

(7) Fleurat-Lessard, P.; Grebenshchikov, S. Y.; Siebert, R.; Schinke, R.; Halberstadt, N. Theoretical investigation of the temperature dependence of the $O + O_2$ exchange reaction. *J. Chem. Phys.* **2003**, *118*, 610−621.

(8) Lin, S. Y.; Guo, H. Quantum statistical study of $O + O_2$ isotopic exchange reactions: Cross sections and rate constants. *J. Phys. Chem. A* **2006**, *110*, 5305−5311.

(9) Schinke, R.; Grebenshchikov, S. Y.; Ivanov, M.; Fleurat-Lessard, P. Dynamical studies of the ozone isotope effect: A status report. *Annu. Rev. Phys. Chem.* **2006**, *57*, 625−661.

(10) Li, Y.; Sun, Z.; Jiang, B.; Xie, D.; Dawes, R.; Guo, H. Communication: Rigorous quantum dynamics of $O + O_2$ exchange reactions on an ab initio potential energy surface substantiate the negative temperature dependence of rate coefficients. *J. Chem. Phys.* **2014**, *141*, 081102.

(11) Sun, Z.; Yu, D.; Xie, W.; Hou, J.; Dawes, R.; Guo, H. Kinetic isotope effect of the $^{16}O + {}^{36}O_2$ and $^{18}O + {}^{32}O_2$ isotope exchange reactions: Dominant role of reactive resonances revealed by an accurate time-dependent quantum wavepacket study. *J. Chem. Phys.* **2015**, *142*, 174312.

(12) Rajagopala Rao, T.; Guillon, G.; Mahapatra, S.; Honvault, P. Quantum dynamics of $^{16}O + {}^{36}O_2$ and $^{18}O + {}^{32}O_2$ exchange reactions. *J. Chem. Phys.* **2015**, *142*, 174311.

(13) Guillon, G.; Honvault, P.; Kochanov, R.; Tyuterev, V. First-Principles Computed Rate Constant for the $O + O_2$ Isotopic Exchange Reaction Now Matches Experiment. *J. Phys. Chem. Lett.* **2018**, *9*, 1931−1936.

(14) Wiegell, M. R.; Larsen, N. W.; Pedersen, T.; Egsgaard, H. The temperature dependence of the exchange reaction between oxygen atoms and dioxygen molecules studied by means of isotopes and spectroscopy. *Int. J. Chem. Kinet.* **1997**, *29*, 745−753.

(15) Anderson, S.; Klein, F.; Kaufman, F. Kinetics of the isotope exchange reaction of $^{18}O$ with NO and $O_2$ at 298 K. *J. Chem. Phys.* **1985**, *83*, 1648−1656.

(16) Fleurat-Lessard, P.; Grebenshchikov, S. Y.; Schinke, R.; Janssen, C.; Krankowsky, D. Isotope dependence of the $O + O_2$ exchange reaction: Experiment and theory. *J. Chem. Phys.* **2003**, *119*, 4700−4712.

(17) Janssen, C.; Guenther, J.; Krankowsky, D.; Mauersberger, K. Temperature dependence of ozone rate coefficients and isotopologue fractionation in $^{16}O-{}^{18}O$ oxygen mixtures. *Chem. Phys. Lett.* **2003**, *367*, 34−38.

(18) Banichevich, A.; Peyerimhoff, S. D.; Grein, F. Potential energy surfaces of ozone in its ground state and in the lowest-lying eight excited states. *Chem. Phys.* **1993**, *178*, 155−188.

(19) Siebert, R.; Schinke, R.; Bittererová, M. Spectroscopy of ozone at the dissociation threshold: Quantum calculations of bound and resonance states on a new global potential energy surface. *Phys. Chem. Chem. Phys.* **2001**, *3*, 1795−1798.

(20) Siebert, R.; Fleurat-Lessard, P.; Schinke, R.; Bittererová, M.; Farantos, S. The vibrational energies of ozone up to the dissociation threshold: Dynamics calculations on an accurate potential energy surface. *J. Chem. Phys.* **2002**, *116*, 9749−9767.

(21) Babikov, D.; Kendrick, B. K.; Walker, R. B.; Pack, R. T.; Fleurat-Lesard, P.; Schinke, R. Metastable states of ozone calculated on an accurate potential energy surface. *J. Chem. Phys.* **2003**, *118*, 6298−6308.

(22) Holka, F.; Szalay, P. G.; Müller, T.; Tyuterev, V. G. Toward an improved ground state potential energy surface of ozone. *J. Phys. Chem. A* **2010**, *114*, 9927−9935.

(23) Dawes, R.; Lolur, P.; Ma, J.; Guo, H. Communication: Highly accurate ozone formation potential and implications for kinetics. *J. Chem. Phys.* **2011**, *135*, 081102.

(24) Lepers, M.; Bussery-Honvault, B.; Dulieu, O. Long-range interactions in the ozone molecule: Spectroscopic and dynamical points of view. *J. Chem. Phys.* **2012**, *137*, 234305.

(25) Ayouz, M.; Babikov, D. Global permutationally invariant potential energy surface for ozone forming reaction. *J. Chem. Phys.* **2013**, *138*, 164311.

(26) Tyuterev, V. G.; Kochanov, R. V.; Tashkun, S. A.; Holka, F.; Szalay, P. G. New analytical model for the ozone electronic ground state potential surface and accurate ab initio vibrational predictions at high energy range. *J. Chem. Phys.* **2013**, *139*, 134307.

(27) Dawes, R.; Lolur, P.; Li, A.; Jiang, B.; Guo, H. Communication: An accurate global potential energy surface for the ground electronic state of ozone. *J. Chem. Phys.* **2013**, *139*, 201103.

(28) Garcia-Fernandez, P.; Bersuker, I. B.; Boggs, J. E. Lost topological (Berry) phase factor in electronic structure calculations. Example: The ozone molecule. *Phys. Rev. Lett.* **2006**, *96*, 163005.

(29) Grebenshchikov, S. Y.; Qu, Z.-W.; Zhu, H.; Schinke, R. New theoretical investigations of the photodissociation of ozone in the Hartley, Huggins, Chappuis, and Wulf bands. *Phys. Chem. Chem. Phys.* **2007**, *9*, 2044−2064.

(30) Alijah, A.; Lapierre, D.; Tyuterev, V. Non-adiabatic coupling in the ozone molecule. *Mol. Phys.* **2018**, *116*, 2660−2670.

(31) Tyuterev, V. G.; Kochanov, R.; Campargue, A.; Kassi, S.; Mondelain, D.; Barbe, A.; Starikova, E.; De Backer, M.; Szalay, P.; Tashkun, S. Does the reef structure at the ozone transition state towards the dissociation exist? New insight from calculations and ultrasensitive spectroscopy experiments. *Phys. Rev. Lett.* **2014**, *113*, 143002.




DOI: 10.1021/acs.jpca.9b06139
J. Phys. Chem. A 2019, 123, 7733−7743

(32) Ndengué, S.; Dawes, R.; Wang, X.-G.; Carrington, T., Jr; Sun, Z.; Guo, H. Calculated vibrational states of ozone up to dissociation. *J. Chem. Phys.* **2016**, *144*, No. 074302.
(33) Lapierre, D.; Alijah, A.; Kochanov, R.; Kokoouline, V.; Tyuterev, V. Lifetimes and wave functions of ozone metastable vibrational states near the dissociation limit in a full-symmetry approach. *Phys. Rev. A* **2016**, *94*, No. 042514.
(34) Tyuterev, V. G.; Kochanov, R. V.; Tashkun, S. A. Accurate ab initio dipole moment surfaces of ozone: First principle intensity predictions for rotationally resolved spectra in a large range of overtone and combination bands. *J. Chem. Phys.* **2017**, *146*, No. 064304.
(35) Campargue, A.; Kassi, S.; Romanini, D.; Barbe, A.; De Backer-Barilly, M.-R.; Tyuterev, V. G. CW-cavity ring down spectroscopy of the ozone molecule in the 6625−6830 $cm^{-1}$ region. *J. Mol. Spectrosc.* **2006**, *240*, 1−13.
(36) Campargue, A.; Barbe, A.; De Backer-Barilly, M.-R.; Tyuterev, V. G.; Kassi, S. The near infrared spectrum of ozone by CW-cavity ring down spectroscopy between 5850 and 7000 $cm^{-1}$: new observations and exhaustive review. *Phys. Chem. Chem. Phys.* **2008**, *10*, 2925−2946.
(37) Barbe, A.; Mikhailenko, S.; Starikova, E.; De Backer, M.-R.; Tyuterev, V. G.; Mondelain, D.; Kassi, S.; Campargue, A.; Janssen, C.; Tashkun, S.; et al. Ozone spectroscopy in the electronic ground state: high-resolution spectra analyses and update of line parameters since 2003. *J. Quant. Spectrosc. Radiat. Transfer* **2013**, *130*, 172−190.
(38) Babikov, Y. L.; Mikhailenko, S. N.; Barbe, A.; Tyuterev, V. G. S&MPO−an information system for ozone spectroscopy on the WEB. *J. Quant. Spectrosc. Radiat. Transfer* **2014**, *145*, 169−196.
(39) Mondelain, D.; Campargue, A.; Kassi, S.; Barbe, A.; Starikova, E.; De Backer, M.-R.; Tyuterev, V. G. The CW-CRDS spectra of the $^{16}O/^{18}O$ isotopologues of ozone between 5930 and 6340 $cm^{-1}$ − Part 1: $^{16}O^{16}O^{18}O$. *J. Quant. Spectrosc. Radiat. Transfer* **2013**, *116*, 49−66.
(40) Barbe, A.; Starikova, E.; De Backer, M.; Tyuterev, V. G. Analyses of infrared FT spectra of asymmetric ozone isotopologue $^{16}O^{16}O^{18}O$ in the range 950−3850 $cm^{-1}$. *J. Quant. Spectrosc. Radiat. Transfer* **2018**, *218*, 231−247.
(41) Campargue, A.; Kassi, S.; Mondelain, D.; Barbe, A.; Starikova, E.; De Backer, M.-R.; Tyuterev, V. G. Detection and analysis of three highly excited vibrational bands of $^{16}O_3$ by CW-CRDS near the dissociation threshold. *J. Quant. Spectrosc. Radiat. Transfer* **2015**, *152*, 84−93.
(42) Starikova, E.; Mondelain, D.; Barbe, A.; Tyuterev, V. G.; Kassi, S.; Campargue, A. CRDS detection and modelling of vibrational bands of $^{18}O_3$ approaching the dissociation threshold (7400−7920 $cm^{-1}$). *J. Quant. Spectrosc. Radiat. Transfer* **2015**, *161*, 203−214.
(43) Feofilov, A. G.; Kutepov, A. A. Infrared radiation in the mesosphere and lower thermosphere: energetic effects and remote sensing. *Surv. Geophys.* **2012**, *33*, 1231−1280.
(44) Manuel, L. P.; Taylor, F. W. *Non-LTE Radiative Transfer in the Atmosphere*; World Scientific: 2001; Vol. 3.
(45) Kaufmann, M.; Gil-López, S.; López-Puertas, M.; Funke, B.; Garcia-Comas, M.; Glatthor, N.; Grabowski, U.; Höpfner, M.; Stiller, G.; Von Clarmann, T.; Koukouli, M. E.; Hoffmann, L.; Riese, M. Vibrationally excited ozone in the middle atmosphere. *J. Atmos. Sol. Terr. Phys.* **2006**, *68*, 202−212.
(46) Hippler, H.; Rahn, R.; Troe, J. Temperature and pressure dependence of ozone formation rates in the range 1−1000 bar and 90−370 K. *J. Chem. Phys.* **1990**, *93*, 6560−6569.
(47) Luther, K.; Oum, K.; Troe, J. The role of the radical-complex mechanism in the ozone recombination/dissociation reaction. *Phys. Chem. Chem. Phys.* **2005**, *7*, 2764−2770.
(48) Teplukhin, A.; Babikov, D. A full-dimensional model of ozone forming reaction: The absolute value of the recombination rate coefficient, its pressure and temperature dependencies. *Phys. Chem. Chem. Phys.* **2016**, *18*, 19194−19206.
(49) Mauersberger, K. Measurement of heavy ozone in the stratosphere. *Geophys. Res. Lett.* **1981**, *8*, 935−937.
(50) Thiemens, M. H.; Heidenreich, J. E. The mass-independent fractionation of oxygen: A novel isotope effect and its possible cosmochemical implications. *Science* **1983**, *219*, 1073−1075.
(51) Gao, Y. Q.; Marcus, R. Strange and unconventional isotope effects in ozone formation. *Science* **2001**, *293*, 259−263.
(52) Grebenshchikov, S. Y.; Schinke, R. Towards quantum mechanical description of the unconventional mass-dependent isotope effect in ozone: Resonance recombination in the strong collision approximation. *J. Chem. Phys.* **2009**, *131*, 181103.
(53) Grebenshchikov, S. Y. A Quantum mechanical study of ozone isotope effect. *Few-Body Syst.* **2009**, *45*, 241−243.
(54) Xie, T.; Bowman, J. M. Quantum inelastic scattering study of isotope effects in ozone stabilization dynamics. *Chem. Phys. Lett.* **2005**, *412*, 131−134.
(55) Marcus, R. A. Theory of mass-independent fractionation of isotopes, phase space accessibility, and a role of isotopic symmetry. *Proc. Natl. Acad. Sci. U. S. A.* **2013**, *110*, 17703−17707.
(56) Thiemens, M. H. Introduction to chemistry and applications in nature of mass independent isotope effects special feature. *Proc. Natl. Acad. Sci. U. S. A.* **2013**, *110*, 17631−17637.
(57) Van Wyngarden, A. L.; Mar, K. A.; Quach, J.; Nguyen, A. P.; Wiegel, A. A.; Lin, S.-Y.; Lendvay, G.; Guo, H.; Lin, J. J.; Lee, Y. T.; Boering, K. A. The non-statistical dynamics of the $^{18}O + {}^{32}O_2$ isotope exchange reaction at two energies. *J. Chem. Phys.* **2014**, *141*, 064311.
(58) Ivanov, M.; Babikov, D. On stabilization of scattering resonances in recombination reaction that forms ozone. *J. Chem. Phys.* **2016**, *144*, 154301.
(59) Teplukhin, A.; Gayday, I.; Babikov, D. Several levels of theory for description of isotope effects in ozone: Effect of resonance lifetimes and channel couplings. *J. Chem. Phys.* **2018**, *149*, 164302.
(60) Teplukhin, A.; Babikov, D. Several Levels of Theory for Description of Isotope Effects in Ozone: Symmetry Effect and Mass Effect. *J. Phys. Chem. A* **2018**, *122*, 9177−9190.
(61) Teplukhin, A.; Babikov, D. Properties of Feshbach and "shape"-resonances in ozone and their role in recombination reactions and anomalous isotope effects. *Faraday Discuss.* **2018**, *212*, 259.
(62) Honvault, P.; Guillon, G.; Kochanov, R.; Tyuterev, V. Quantum mechanical study of the $^{16}O + {}^{18}O^{18}O \rightarrow {}^{16}O^{18}O + {}^{18}O$ exchange reaction: Integral cross sections and rate constants. *J. Chem. Phys.* **2018**, *149*, 214304.
(63) Ruscic, B. Unpublished results obtained from active thermochemical tables (ATcT) based on the Core (Argonne) Thermochemical Network version 1.110, 2010.
(64) Werner, H.-J.; Knowles, P. J.; Knizia, G.; Manby, F. R.; Schütz, M. Molpro: a general-purpose quantum chemistry program package. *WIREs. Comput. Mol. Sci.* **2012**, *2*, 242−253.
(65) Ruscic, B.; Pinzon, R. E.; Morton, M. L.; von Laszevski, G.; Bittner, S. J.; Nijsure, S. G.; Amin, K. A.; Minkoff, M.; Wagner, A. F. Introduction to active thermochemical tables: Several key enthalpies of formation revisited. *J. Phys. Chem. A* **2004**, *108*, 9979−9997.
(66) Hernandez-Lamoneda, R.; Salazar, M. R.; Pack, R. Does ozone have a barrier to dissociation and recombination? *Chem. Phys. Lett.* **2002**, *355*, 478−482.
(67) Van Wyngarden, A. L.; Mar, K. A.; Boering, K. A.; Lin, J. J.; Lee, Y. T.; Lin, S.-Y.; Guo, H.; Lendvay, G. Nonstatistical behavior of reactive scattering in the $^{18}O + {}^{32}O_2$ isotope exchange reaction. *J. Am. Chem. Soc.* **2007**, *129*, 2866−2870.
(68) Lischka, H.; Müller, T.; Szalay, P. G.; Shavitt, I.; Pitzer, R. M.; Shepard, R. Columbus A program system for advanced multireference theory calculations. *WIREs. Comput. Mol. Sci.* **2011**, *1*, 191−199.
(69) Tyuterev, V. G.; Barbe, A.; Jacquemart, D.; Janssen, C.; Mikhailenko, S. N.; Starikova, E. N. Ab initio predictions and laboratory validation for consistent ozone intensities in the MW, 10 and 5 μm ranges. *J. Chem. Phys.* **2019**, *150*, 184303.
(70) Meyer, H.-D.; Manthe, U.; Cederbaum, L. S. The Multi-Configurational Time-Dependent Hartree Approach. *Chem. Phys. Lett.* **1990**, *165*, 73−78.


DOI: 10.1021/acs.jpca.9b06139
J. Phys. Chem. A 2019, 123, 7733−7743

(71) Manthe, U.; Meyer, H.-D.; Cederbaum, L. S. Multiconfigurational Time-Dependent Hartree Study of Complex Dynamics: Photodissociation of $NO_2$. *J. Chem. Phys.* **1992**, *97*, 9062−9071.
(72) Beck, M. H.; Jäckle, A.; Worth, G.; Meyer, H.-D. The multiconfiguration time-dependent Hartree (MCTDH) method: a highly efficient algorithm for propagating wavepackets. *Phys. Rep.* **2000**, *324*, 1−105.
(73) *Multidimensional Quantum Dynamics: MCTDH Theory and Applications*; Meyer, H.-D., Gatti, F., Worth, G. A., Eds.; Wiley-VCH: Weinheim, 2009.
(74) Echave, J.; Clary, D. C. Potential optimized discrete variable representation. *Chem. Phys. Lett.* **1992**, *190*, 225.
(75) Wei, H.; Carrington, T., Jr. The discrete variable representation of a triatomic Hamiltonian in bond lengthbond angle coordinates. *J. Chem. Phys.* **1992**, *97*, 3029.
(76) Jäckle, A.; Meyer, H.-D. Product representation of potential energy surfaces. *J. Chem. Phys.* **1996**, *104*, 7974.
(77) Jäckle, A.; Meyer, H.-D. Product representation of potential energy surfaces II. *J. Chem. Phys.* **1998**, *109*, 3772.
(78) Gatti, F.; Meyer, H.-D. Intramolecular Vibrational Energy Redistribution in Toluene: A nine dimensional Quantum mechanical study using the MCTDH algorithm. *Chem. Phys.* **2004**, *304*, 3−15.
(79) Pasin, G.; Gatti, F.; Iung, C.; Meyer, H.-D. Theoretical investigation of Intramolecular Vibrational Energy Redistribution in highly excited HFCO. *J. Chem. Phys.* **2006**, *124*, 194304.
(80) Ndengué, S. A.; Dawes, R.; Gatti, F.; Meyer, H.-D. Resonances of HCO Computed Using an Approach Based on the Multiconfiguration Time-Dependent Hartree Method. *J. Phys. Chem. A* **2015**, *119*, 12043−12051.
(81) Leforestier, C.; Wyatt, R. E. Optical potential for laser induced dissociation. *J. Chem. Phys.* **1983**, *78*, 2334.
(82) Kosloff, R.; Kosloff, D. Absorbing boundaries for wave propagation problems. *J. Comput. Phys.* **1986**, *63*, 363.
(83) Riss, U. V.; Meyer, H.-D. Calculation of resonance energies and widths using the complex absorbing potential method. *J. Phys. B: At., Mol. Opt. Phys.* **1993**, *26*, 4503.
(84) Riss, U. V.; Meyer, H.-D. Investigation on the reflection and transmission properties of complex absorbing potentials. *J. Chem. Phys.* **1996**, *105*, 1409.
(85) Vibok, A.; Balint-Kurti, G. G. Reflection and transmission of waves by a complex potential, a semiclassical Jeffreys-Wentzel-Kramers-Brillouin treatment. *J. Chem. Phys.* **1992**, *96*, 7615.
(86) Jäckle, A.; Heitz, M.-C.; Meyer, H.-D. Reaction cross sections for the H + $D_2$ ($\nu$ = 0,1) system for collision energies up to 2.5 eV: A multiconfiguration time-dependent Hartree wave-packet propagation study. *J. Chem. Phys.* **1999**, *110*, 241−248.
(87) Tannor, D. J.; Weeks, D. E. Wave packet correlation function formulation of scattering theory: The quantum analog of classical S-matrix theory. *J. Chem. Phys.* **1993**, *98*, 3884−3893.
(88) Rao, T. R.; Guillon, G.; Mahapatra, S.; Honvault, P. Differential cross sections and product rovibrational distributions for $^{16}O + {}^{32}O_2$ and$^{18}O + {}^{36}O_2$ collisions. *J. Phys. Chem. A* **2015**, *119*, 11432−11439.
(89) Pechukas, P.; Light, J. C.; Rankin, C. Statistical Theory of Chemical Kinetics: Application to Neutral-Atom—Molecule Reactions. *J. Chem. Phys.* **1966**, *44*, 794−805.
(90) Miller, W. H. Study of the statistical model for molecular collisions. *J. Chem. Phys.* **1970**, *52*, 543−551.
(91) Sun, Z.; Liu, L.; Lin, S. Y.; Schinke, R.; Guo, H.; Zhang, D. H. State-to-state quantum dynamics of O + $O_2$ isotope exchange reactions reveals nonstatistical behavior at atmospheric conditions. *Proc. Natl. Acad. Sci. U. S. A.* **2010**, *107*, 555−558.
(92) Townsend, D.; Lahankar, S. A.; Lee, S. K.; Chambreau, S. D.; Suits, A. G.; Zhang, X.; Rheinecker, J.; Harding, L.; Bowman, J. M. The roaming atom: straying from the reaction path in formaldehyde decomposition. *Science* **2004**, *306*, 1158−1161.
(93) Bowman, J. M. *Mol. Phys.* **2014**, *112*, 2516−2528.
(94) Mauguière, F. A.; Collins, P.; Kramer, Z. C.; Carpenter, B. K.; Ezra, G. S.; Farantos, S. C.; Wiggins, S. Phase space barriers and dividing surfaces in the absence of critical points of the potential energy: Application to roaming in ozone. *J. Chem. Phys.* **2016**, *144*, 054107.



DOI: 10.1021/acs.jpca.9b06139
*J. Phys. Chem. A* 2019, 123, 7733−7743